Journal of Renewable Materials

Tech Science Press

DOI: 10.32604/jrm.2023.027852

ARTICLE

Preparation of Iron-Pillared Bentonite/Oyster Shell Composite and Phosphate Adsorption in Water

Zhijian Zhou[1], Jie Yan[1,*], Xinxiang Du[1], Qiulin Xu[1], Zijun Wu[2], Jinlan Yang[3], Xitong Fang[1], Qiuling Zhong[2] and Qiaoguang Li[1,*]

[1]College of Chemistry and Chemical Engineering, Zhongkai University of Agriculture and Engineering, Guangzhou, 510225, China

[2]College of Light Industry and Food Science, Zhongkai University of Agriculture and Engineering, Guangzhou, 510225, China

[3]Building Energy Efficiency Research Institute, Guangdong Provincial Academy of Building Research Group Co, Ltd., Guangzhou, 510500, China

[*]Corresponding Authors: Jie Yan. Email: yanjie0001@126.com; Qiaoguang Li. Email: liqiaoguang8799@163.com

Received: 17 November 2022 Accepted: 27 December 2022 Published: 20 July 2023

ABSTRACT

Iron-pillared bentonite (FB) was prepared by Fe(III) modified bentonite, and then the composites (FB-OS) were prepared by iron-pillared bentonite and oyster shell powder. The composites were characterized by FTIR, SEM, TGA, and EDS, and the phosphorus removal test was carried out. The results showed that FB-OS contained a large amount of CaO. Its structure was compact, but there were gaps in it. The maximum bending stress and compressive strength were 43.7 N and 0.927 MPa, respectively. The phosphorus removal test showed that the phosphorus removal rate of FB-OS was more than 90%, and measured the maximum adsorption capacity was 48.31 mg/g. A large amount of spherical products were produced on the surface and inside of FB-OS after phosphorus removal, it was speculated that spherical products were amorphous calcium phosphate in the paper. Analysis indicated that there was chemical adsorption during phosphorus removal. The kinetic equation of phosphorus adsorption by FB-OS was $q_t = \frac{10.193t}{1 + 2.574t}$ (R^2 = 0.995). The adsorption rate was mainly controlled by outer film diffusion and intraparticle diffusion.

KEYWORDS

Oyster shell powder; iron-pillared bentonite; composite material; phosphorous removal

---

Nomenclature

OS	Oyster shell powder
CB	Calcium bentonite
FB	Iron-pillared bentonite
FB-OS	Iron-pillared bentonite/oyster shell powder composite material

1 Introduction

In the world, a large number of oysters are produced and consumed every year (South Korea and the United States produced 298,973 tons and 141,027 tons in 2016, respectively) [1], and then a larger amount of oyster shells are produced. At present, most oyster shells are landfilled, occupying limited urban space and causing a waste of precious resources. The content of $CaCO_3$ in oyster shells is about 90%, and it also contains iron, magnesium, aluminum, and other trace metal elements, polysaccharides, and 16 kinds of amino acids [2,3]. It can be used in building materials, feed additives, and water treatment [4–6], among which water treatment has become a research hotspot due to its large dosage.

The oyster shell has a microporous structure and a large amount of $CaCO_3$, which can be combined with phosphorus in water to form more insoluble $Ca_3(PO_4)_2$, reducing the concentration of phosphorus in water [7]. However, the adsorption of natural oyster shell powder was slow, the adsorption capacity was low, and the concentration of phosphorus in water was still high after treatment [8,9]. Some scholars have modified it to enhance its phosphorus removal performance. According to the existing literature, the modification of oyster shell powder can be divided into three categories: thermal modification, metal compound modification, and clay modification. Thermal modification is to calcine at high temperatures. $CaCO_3$ in oyster shell powder was decomposed into CaO and CO_2 [10]. The products had good phosphorus removal performance, but the particle size was small and could easily lead to filter clogging (The solution after phosphorus removal was not colorless and transparent). In view of this shortcoming, some studies have introduced metal compounds to increase the particle size of precipitated particles. Metal compounds were mixed with calcined oyster shell powder (solid-solid) to produce composite materials for phosphorus removal. Flocculation performance of metal compounds could increase the particle size of the precipitated particles, commonly used iron, aluminum, Lanthanum, and other compounds in literature reports. Among them, iron and aluminum compounds modified oyster shell powder, Fe^{3+} and Al^{3+} in composite materials had strong flocculation performance, and Fe^{3+}/Ca^{2+} had synergistic effects in the phosphorus removal process. These methods increased the particle size of precipitated particles, and enhanced phosphorus removal performance [11,12]. About lanthanum compounds, La^{3+} had an anti-interference ability. Lanthanide compounds modified oyster shell powder could broaden the optimal pH range of solution to be treated [13]. The composite materials prepared by these methods had good phosphorus removal performance, and the precipitate particles became larger, but there were still a large number of fine precipitates, which cannot completely solve the problem of filter blockage caused by small particle size.

In order to further solve the problem of small particle size of precipitated particles, some scholars have studied the oyster shell powder by adding an additive with cohesiveness and plasticity, and then mixtures calcined to prepare a granular material. Bentonite as a clay has a wide source, large reserves, a certain degree of adhesion, plasticity, and ion exchange capacity [14], and it was commonly used in material preparation [15,16]. Materials made from bentonite often had good mechanical properties [17]. However, the adsorption performance of bentonite was not good. Some scholars have studied the way of pillaring metal ions such as Fe^{3+}, Al^{3+}, and Mg^{2+} to enhance their adsorption performance, and the phosphorus removal test achieved good results [18,19].

Regarding modification of oyster shell powder, the above analysis showed that thermal modification and metal compound modification could improve its phosphorus removal performance, and bentonite modification could obtain products with good mechanical properties. Can phosphorus removal materials with excellent performance be prepared if these modification methods were organically combined? After retrieval, there is no relevant literature reported. Therefore, the paper used metal compound pillaring technology to introduce iron ions to bentonite, and then iron-pillared bentonite was mixed with oyster shell powder, granulated and calcined to obtain granular materials. The samples were characterized by FTIR, SEM, TGA, and EDS, and the phosphorus removal test was carried out using an artificial phosphorus solution. The paper expects to use oyster shell waste to prepare phosphorus removal materials with good performance.

2 Experience

2.1 Materials and Instruments

Oyster shell powder (particle size is 120 mess, Yangxi Chengcun Haizhuzi Oyster Co., Ltd., Yangjiang, China); Calcium bentonite (particle size is 200 mess, Lingshou Dehang Mineral Products Co., Ltd., Shijiazhuang, China); $Fe_2(SO_4)_3$ (AR, Shanghai McLin Biochemical Technology Co., Ltd., Shanghai, China); NaOH (AR, Xilong Science Co., Ltd., Guangzhou, China); $NaH_2PO_4·2H_2O$ (AR, Guangdong Guanghua Technology Co., Ltd., Guangzhou, China); Ascorbic acid (AR, Tianjin Damao Chemical Reagent Factory, Tianjin, China); $(NH_4)_2MoO_4$ (AR, Tianjin Baishi Chemical Co., Ltd., Tianjin, China); HCl (36%~38%, Shanxi Xinshunyuan, Jinzhong, China); Deionized water (laboratory homemade).

UV-5100B UV visible spectrophotometer (Shanghai Yuanxi Instrument Co., Ltd., Shanghai, China); TGA2 synchronous thermal analyzer (TA, New Castle, USA); EVO18 scanning electron microscope (Zeiss, Oberkochen, Germany); BSX2-5-12P muffle furnace (Shanghai Yiheng Technology Co., Ltd., Shanghai, China); Spectrum 100 FTIR (Perkin Elmer Inc., Waltham, USA); Hand-shaking granulator (Shanghai Zhenyue Trading Co., Ltd., Shanghai, China).

2.2 Sample Preparation

(1) Preparation of iron-pillared bentonite

According to the literature and slightly improved [20], the preparation method of iron-pillared bentonite was as follows: The iron-pillared liquid was prepared by n (OH^-): n (Fe^{3+}) = 1: 1.5. 100 g calcium bentonite was dispersed into 2.0 L deionized water, and the iron-pillared liquid was added to the calcium bentonite solution to reach 10 mmol/g. The other operations (such as filtering, washing, and drying) were the same as those in the literature, and the iron-pillared bentonite (FB) was finally obtained.

(2) Preparation of iron-pillared bentonite/oyster shell composite

The oyster shell powder and iron-pillared bentonite were fully mixed at a mass ratio of 3:1 (B-FB-OS). An appropriate amount of deionized water was added into mixed powder to get muddy solid. The muddy solid granulated by hand-shaking granulator (cylinder diameter 5 mm, height 6~7 mm) to obtain granular materials. The granular materials dried at 105°C for 1 h, and then transferred to a muffle furnace at 11°C/min to 700°C and held for 1 h. Naturally cooling in the muffle furnace, the composites iron-pillared bentonite/oyster shell powder composite (FB-OS) were finally obtained.

2.3 Sample Characterization

(a) Fourier transform infrared spectroscopy (FTIR)

The sample to be tested was added with KBr powder, pressed, and scanned at 450~4000 cm^{-1} band.

(b) Thermal stability analysis (TGA)

The temperature program was set (temperature range of 40°C–800°C, nitrogen heating rate of 10°C/min). 3~5 mg sample was placed in the instrument. Temperature programmed to obtain TGA, and DTG obtained by TGA mathematical processing.

(c) Scanning electron microscope (SEM)

After the pretreatment of the sample to be tested, it was placed in the instrument, and the high-energy particles impacted the surface to observe the surface morphology of the sample.

(d) Energy dispersive spectrometer (EDS)

The composition and content of elements in the sample were analyzed by using the characteristic energy of X-ray photons of different elements.

(e) Determination of particle strength

The samples were placed on the instrument and compressed from top to bottom until the particles were damaged. The maximum bending stress was recorded and paralleled for 15 times. The compressive strength σ_c (Pa) was calculated by formula (1).

$$\sigma_c = \frac{2 \cdot F}{\pi \cdot T \cdot L} \tag{1}$$

where T (m) is the diameter of the cylinder; L (m) is the length of the cylinder; F (N) is the maximum bending stress.

2.4 *Phosphorus Removal Test*

(1) Operation process

Standard phosphorus solution (5.00 g/L) was prepared. Phosphorus solutions of other concentrations (5~150 mg/L) were prepared by diluting with 5.00 g/L standard phosphorus solution in the experiment.

The phosphorus removal performance test of composite materials was as follows: The phosphorus solution was added to a glass reagent bottle. FB-OS was added into above solution, and FB-OS statically adsorbed phosphorus from solution in a constant temperature water bath. Test water samples were taken at 3~5 cm below the liquid level on time, and they filtered by 0.45 μm filter membrane. The concentrations in the filtrate were determined. Single factor experiments were carried out on adsorption time, water bath temperature, amount of adsorption materials and different initial concentrations of phosphorus.

(2) Determination of phosphorus content in solution

The content of phosphorus in water was determined by HCl-ammonium molybdate-spectrophotometer method according to the literature [21]. The standard curve of phosphorus concentration was obtained: $A = 0.00211c + 0.000292683$ ($R^2 = 0.9996$), where A is absorbance and c is phosphorus concentration (mg/L).

(a) Phosphorus removal rate

$$R = \frac{c_t}{c_0} \times 100\% \tag{2}$$

where R (%) is the removal rate of phosphorus; c_0 and c_t (mg/L) are the initial phosphorus concentration and t (h) concentration, respectively.

(b) Phosphorus adsorption capacity

$$q = \frac{(c_0 - c_t)V}{m} \tag{3}$$

where q (mg/g) is the adsorption amount of phosphorus; V (L) is the volume of phosphorus solution; m (g) is the mass of the sample.

2.5 *Adsorption Kinetic Equation*

In order to explore the adsorption behavior of FB-OS, pseudo-first-order kinetics and pseudo-second-order kinetics equations were fitted for its adsorption curve [22–24]. The equation was as follows:

Pseudo-first-order kinetics equation (PFO) [25]:

$$q_t = q_e\left(1 - e^{-k_1 t}\right) \tag{4}$$

The logarithm of formula (4) is transformed into:

$$lg(q_e - q_t) = lg(q_e) - \frac{k_1 t}{2.303} \tag{5}$$

Pseudo-second-order kinetic equation (PSO) [25]:

$$q_t = \frac{q_e^2 k_2 t}{1 + q_e k_2 t} \tag{6}$$

Formula (6) is transformed into:

$$\frac{t}{q_t} = \frac{1}{k_2 q_e^2} + \frac{t}{q_e} \tag{7}$$

where q_e and q_t (mg/g) are the adsorption capacity of the adsorbent at equilibrium; t (h) is adsorption time; k_1 (h^{-1}) and k_2 (g/(mg·h)) are rate constants.

3 Result

3.1 Characterization of Materials

3.1.1 FTIR Results and Analysis

Fig. 1 is the infrared spectra of raw materials and products. According to the figure, both calcium bentonite and iron-pillared bentonite contained the characteristic peaks of 2829 cm^{-1} ($-CH_3$ symmetrical stretching vibration peak) and 1367 cm^{-1} (C-H bending vibration peak). Among them, calcium bentonite also contained the characteristic peak of 2740 cm^{-1} ($-CH_2$ symmetrical stretching vibration peak), and iron-pillared bentonite had the characteristic peaks of 2952 cm^{-1} ($-CH_3$ asymmetric tensile vibration peak) and 2660 cm^{-1} ($-CH_2$ symmetrical stretching vibration peak) [26]. The above proved that calcium bentonite and iron-pillared bentonite both contained organic matter, and showed that the iron-pillared modification process did not completely wash away the original organic matter of calcium bentonite. Meanwhile, calcium bentonite and iron-pillared bentonite also contained 1105 cm^{-1} (Si-O stretching vibration peak in quartzite), 1034 cm^{-1} (Si-O stretching vibration peak), 508 cm^{-1} (low-frequency Si-O vibration), and 472 cm^{-1} (Si-O-Fe bending vibration peak) characteristic peaks, indicating that both contained SiO_2 and $Fe_2(SiO_3)_3$ [27]. Compared with calcium bentonite, iron-pillared bentonite had several obvious differences. Iron-pillared bentonite had 618 cm^{-1} (Si-O-Al bending vibration peak) and 1443 cm^{-1} (CO_3^{2-} stretching of calcite) characteristic peaks, on the base of the reports [28,29], which explained that iron-pillared bentonite contained $Al_2(SiO_3)_3$ and $CaCO_3$. The iron-pillared bentonite formed an obvious characteristic absorption peak of $Fe(OH)_3$ hydroxyl group at 771 cm^{-1}, which was the most obvious difference with calcium bentonite. Combined with the literature analysis, this may be caused by the intercalation of Fe(III) in the iron-pillared liquid into the bentonite interlayer during the modification of calcium bentonite [30,31]. It evidenced that the iron-pillared bentonite was successfully prepared in this experiment. Fig. 1 also showed that oyster shell powder had characteristic peaks of 2752 cm^{-1}, 1443 cm^{-1}, 1034 cm^{-1}, and 870 cm^{-1} (Ca-O stretching vibration peak), which explained that oyster shell powder contained organic matter, SiO_2, and $CaCO_3$ [31,32]. This was because of the contamination from impurities such as soil or cement during oyster farming, and oyster shell pretreatment did not completely remove impurities, resulting in oyster shell powder containing SiO_2. FB-OS (Fig. 1) had characteristic peaks of 2952 cm^{-1}, 2829 cm^{-1}, 2714 cm^{-1}, and 1367 cm^{-1}. This expressed that there was still incompletely decomposed organic matter in the particles after calcination. FB-OS also contained

1135 cm^{-1}, 963 cm^{-1} (Al-Al-OH), 870 cm^{-1}, 711 cm^{-1} and 534 cm^{-1}, meaning that FB-OS also contained CaO, $CaCO_3$, Al_2O_3, MgO and SiO_2. FB-OS did not form a new characteristic peak. However, in the literature [33], CaO produced by the decomposition of oyster shell powder reacted with SiO_2 to form $CaSiO_3$ at high temperatures. This may produce too little $CaSiO_3$ to be shown in Fig. 1. In summary, the organic matter was not completely decomposed during the calcination process, and Fe(III) was successfully embedded into the calcium bentonite interlayer, and some oyster shell powder was pyrolyzed to generate CaO at high temperature.

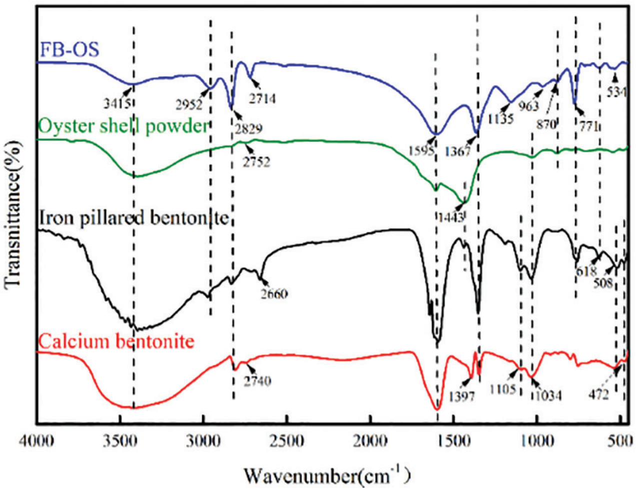

Figure 1: FTIR of calcium bentonite, iron-pillared bentonite, oyster shell powder and FB-OS

3.1.2 Results and Analysis of TGA and DTG

The thermal analysis of oyster shell powder, iron-pillared bentonite, B-FB-OS, and FB-OS was carried out, and the results were shown in Figs. 2a, 2b. Weight loss before 100°C was caused by each substance's volatilization of free water [34]. A small weight loss peak was formed near 120°C, this was attributed to the volatilization of bound water in iron-pillared bentonite and B-FB-OS at high temperatures [35]. B-FB-OS had a small weight loss peak near 349°C, and iron-pillared bentonite also had a small weight loss peak at 358°C. According to the literature [36], this peak was the dehydration of -OH and -COOH in organic matter at high temperatures. This indicated that iron-pillared bentonite contained organic matter. B-FB-OS had a small weight loss peak near 483°C, and iron-pillared bentonite also had a small weight loss peak at 593°C. These peaks were the weight loss peak of $Fe(OH)_3$ and $Al(OH)_3$, removing H_2O to form Fe_2O_3 and Al_2O_3 at high temperatures [36,37]. Among them, the ratio of impurity in the sample might be effecting the dehydration temperature of $Al(OH)_3$ and $Fe(OH)_3$ in the sample during calcination [38,39]. Thus, dehydration temperature of metal compounds decreased in B-FB-OS. Oyster shell powder, B-FB-OS and FB-OS had a significant weight loss peak at 730°C, 718°C and 709°C, respectively, which was due to the mass loss caused by the thermal decomposition of $CaCO_3$ in oyster shell powder into CaO and CO_2. The weight loss peak temperature of $CaCO_3$ in B-FB-OS and FB-OS was lower than that of oyster shell powder because of the presence of metal ions such as Al^{3+} in clay, Al^{3+} promoted the decomposition of $CaCO_3$ [40–42]. The difference between B-FB-OS and FB-OS may be caused by the different relative content of Al^{3+}. The temperature of water volatilization and organic matter decomposition was lower than 560°C. Above 560°C, only $CaCO_3$ decomposition led to weight loss. At 560°C~800°C, the weight loss rates of oyster shell powder, B-FB-OS and FB-OS were 37.68%, 25.91%, and 19.82%, respectively. The weight loss rate of FB-OS was compared with that of oyster shell powder and B-FB-OS, which explained that only part of $CaCO_3$ decomposed during the calcination process, and a large amount of undecomposed $CaCO_3$ remained in the composite. In conclusion, there was decomposition of organic compounds, dehydration of metal hydroxides, and $CaCO_3$ pyrolysis in the process of calcination.

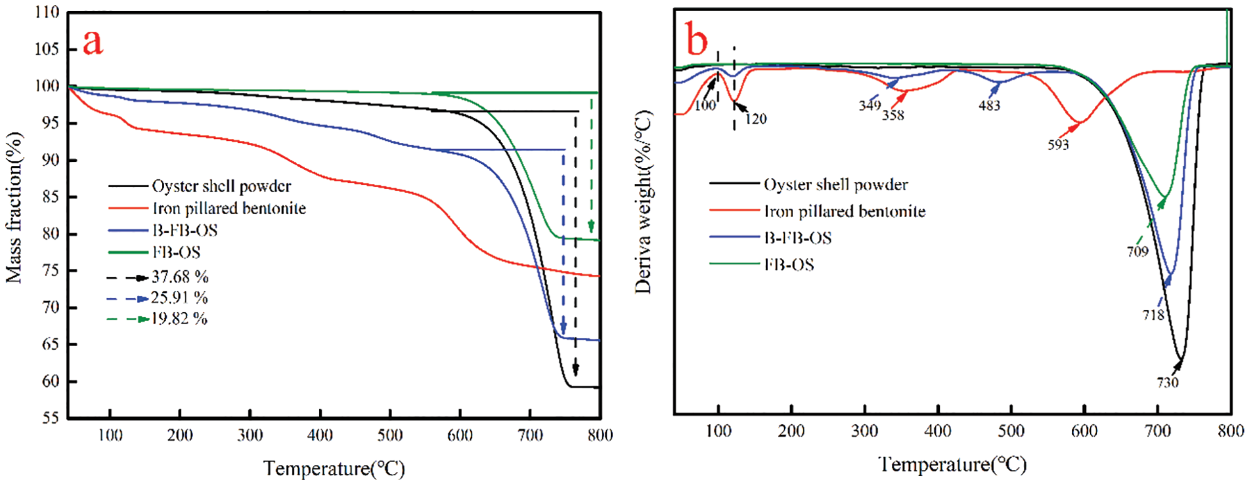

Figure 2: Thermogravimetric analysis diagram (a is the TGA diagram of raw materials and products, b is the DTG diagram of raw materials and products)

3.1.3 Results and Analysis of SEM and EDS

Fig. 3 is the SEM diagram of calcium bentonite, iron-pillared bentonite and FB-OS before and after phosphorus removal. It can be seen that there was a leaf-like texture on the surface of calcium bentonite, and calcium bentonite was composed of leaf-like blocks [43]. The iron-pillared bentonite (Fig. 3b) was also a leaf-like stacking structure, which showed that the effect of modification on the structure of calcium bentonite was not significant. In order to further explore the element composition of iron-pillared bentonite, its SEM diagram (Fig. 3b) was analyzed by EDS, and the results were shown in Fig. 4a. The characteristic peaks of Fe, C, O, Na, Al, S, Mg, K, Si and Ca were observed on EDS. The characteristic peaks of C, S, and O indicated that iron-pillared bentonite contained organic matter. The characteristic peak of Si proved that iron-pillared bentonite contained SiO_2. The characteristic peaks of K, Mg, Ca, Al, Fe, and Na indicated that iron-pillared bentonite contained a variety of minerals. In particular, Fig. 4b showed that the weight percentage of iron in iron-pillared bentonite was 24.67%. According to the literature [44], the highest weight percentage of Fe_2O_3 in calcium bentonite was about 8.6%. Relatively speaking, the iron content in the iron-pillared bentonite had been significantly improved, which indicated that some Fe(III) may be successfully embedded in the interlayer of calcium bentonite.

Fig. 3c showed that the FB-OS structure was compact but with gaps. The compact structure of FB-OS was due to the good plasticity and adhesion of iron-pillared bentonite, it made up for the disadvantage that oyster shell powder cannot be formed. In addition, the compact structure was one of the reasons why the composite material had good mechanical properties. The maximum bending stress of FB-OS measured by the particle strength tester was 43.7 N and the compressive strength was 0.927 Mpa. Of course, iron-pillared bentonite also contributed to the mechanical properties of the material. Needle-like crystals could be observed inside the material (Fig. 3d). According to the literature [33,45], it was speculated that needle-like crystals may be goethite or hydrated calcium silicate. However, the characterization results of this paper failed to confirm which substance it was, so the structure needs further research and analysis. After phosphorus removal, a large number of spherical products were formed on the surface of FB-OS (Fig. 3d), and they were characterized by EDS. The EDS results showed that the spherical products contained C, K, Mg, Na, Ca, O, Fe, Al, S, P and Si elements (Fig. 4c), and the mass percentages of Ca, O and P were 19.51%, 30.02% and 4.04%, respectively (Fig. 4d). On based of the literature [46,47], amorphous calcium phosphate was composed of Ca, O and P elements, and its morphology under electron microscope was spherical. Based on the above analysis, it was speculated that the spherical product was amorphous calcium phosphate in this experiment. This indicated that PO_4^{3-} (HPO_4^{2-} and H_2PO^-) in phosphorus solution reacted with Ca^{2+} to form Ca_3 $(PO_4)_2$ ($CaHPO_4$ and $Ca(H_2PO_4)_2$), and the products adhered to the surface of the adsorbent. The spherical product also contained C, Fe, Al, S, K, Na, Mg, and Si elements. It was possible that the amorphous calcium phosphate was doped with $FePO_4$, $AlPO_4$ and iron-pillared bentonite during the formation. Spherical products could also be observed inside FB-OS (Fig. 3e), which was the same as the spherical products on the surface (Fig. 3d). This showed that phosphorus could enter into the interior of the composite material along the gap during the phosphorus removal process, and reacted with Ca^{2+} to form amorphous calcium phosphate.

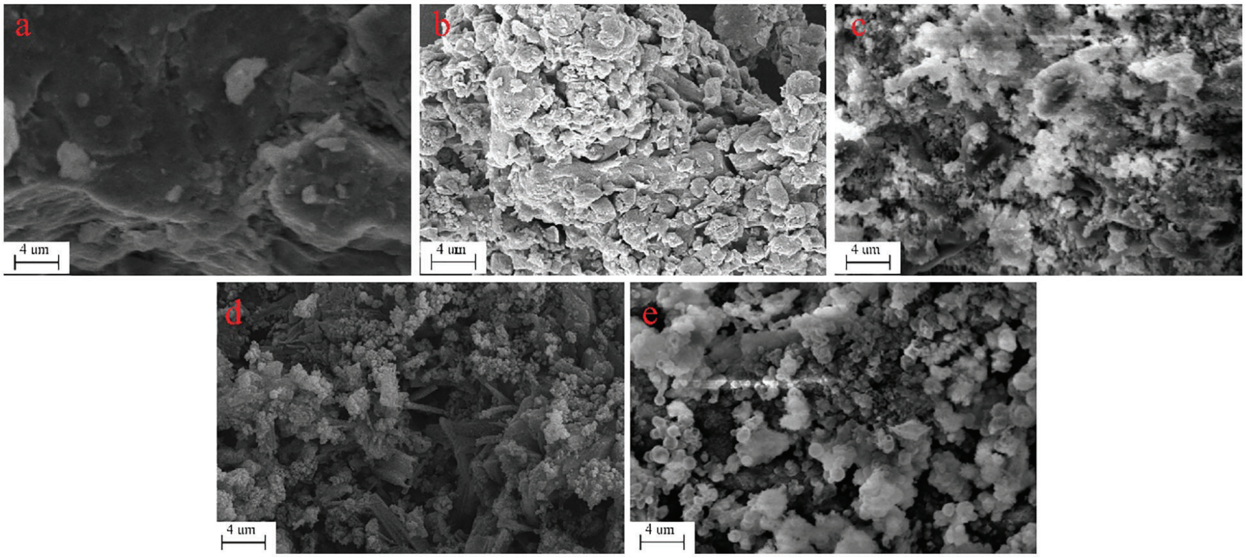

Figure 3: SEM of each substance (a is calcium bentonite, b is iron-pillared bentonite, c is the internal structure of FB-OS before phosphorus removal, d is the surface structure of FB-OS after phosphorus removal, e is the internal structure of FB-OS after phosphorus removal)

3.2 Phosphorus Adsorption Experiment

3.2.1 Effect of Temperature on Phosphorus Removal Performance of FB-OS

Fig. 5a showed the results of different temperatures on the phosphorus removal performance of FB-OS. The experimental conditions were an initial phosphorus concentration of 150 mg/L and a water volume of 50 mL. Before 5 h, the figure showed that although the adsorption rate at 40°C was higher than that at 30°C, the difference between the two could be ignored, and they were slightly higher than 20°C. This was because the increase of temperature accelerated the movement of ions in the system, which increased the contact probability between PO_4^{3-} and the active sites. That was conducive to the adsorption of phosphorus by FB-OS [48]. After 5 h, the adsorption of phosphorus by FB-OS tended to be at equilibrium under three temperature conditions. At 30 h, the adsorption capacities at 20°C, 30°C and 40°C were 3.48, 3.69 and 3.65 mg/g, respectively. At this time, the phosphorus removal rates all were higher than 90%. Based on the above analysis, under the experimental conditions, high temperature could accelerate the adsorption of phosphorus by FB-OS, but the increase was not significant, and the temperature had no significant effect on adsorption capacity and phosphorus removal rate. Therefore, it is suitable to choose room temperature in practical applications.

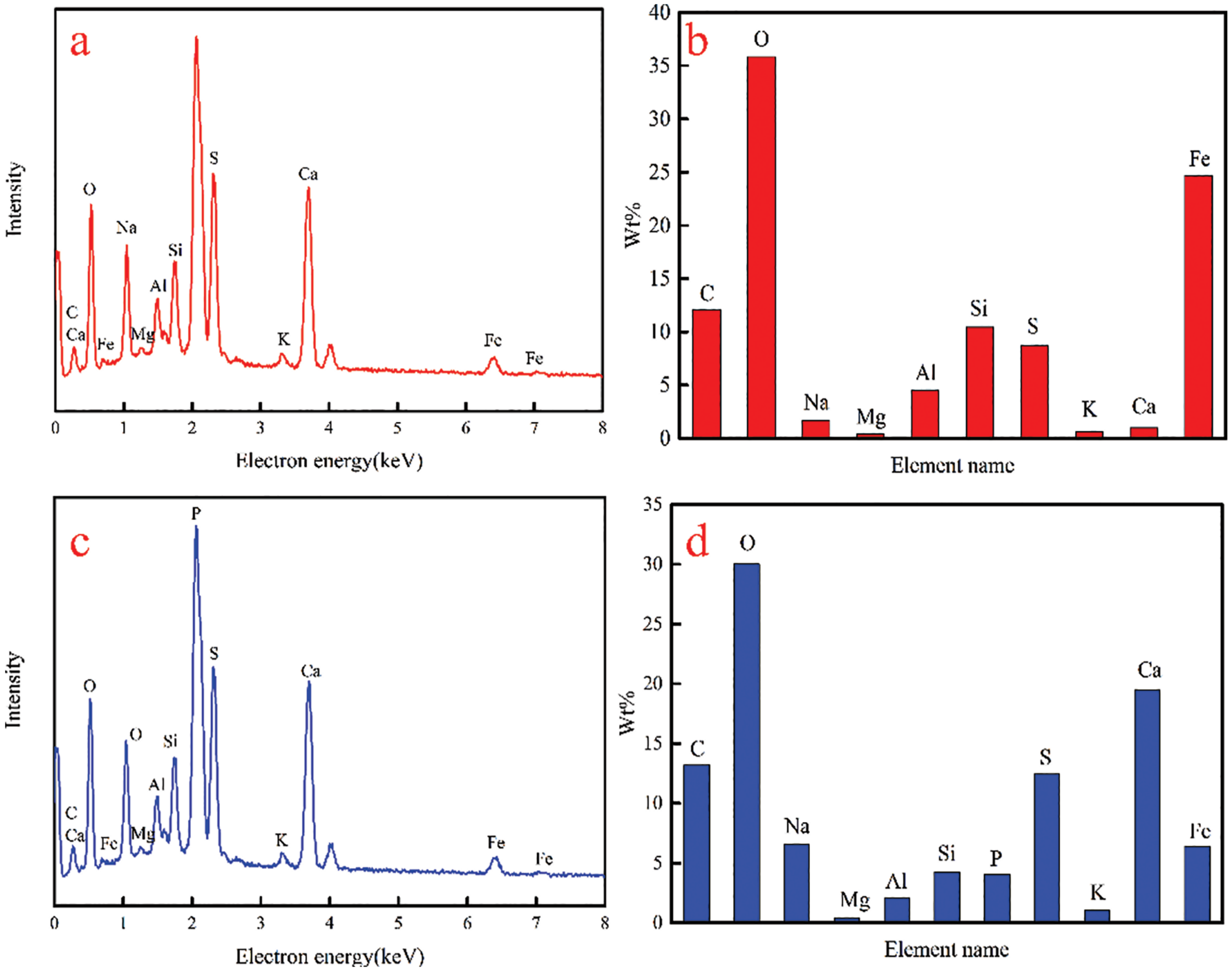

Figure 4: Electron diffraction spectra of iron-pillared bentonite and spherical products (a, b are EDS of iron-pillared bentonite, c, d are EDS of spherical products)

3.2.2 Effect of FB-OS Dosage on Phosphorus Removal Performance

At room temperature, different amounts of FB-OS were added to 200 mL aqueous solution with an initial phosphorus concentration of 150 mg/L, and test water samples were taken after 2 d. The results were shown in Fig. 5b. As can be seen from the figure, the influence of FB-OS dosage on phosphorus adsorption could be roughly divided into two situations: 0~3 g and above 3 g. The dosage of FB-OS was 0~3 g. With the increase of FB-OS dosage, the active center increased, Ca^{2+}/PO_4^{3-} increased, the probability of Ca^{2+} contacting with PO_4^{3-} (HPO_4^{2-} and $H_2PO_4^{-}$) increased, and the removal rate increased [11,49]. The amount of adsorbent was 3 g, and the phosphorus removal rate reached 99.46%. When FB-OS was further increased, the dosage was greater than the demand for phosphorus removal, and the phosphorus removal rate was no longer significantly improved. Therefore, the optimum dosage of FB-OS was 3 g. Under this condition, the adsorption capacity of phosphorus was 9.93 mg/g, and the removal rate was 99.46%.

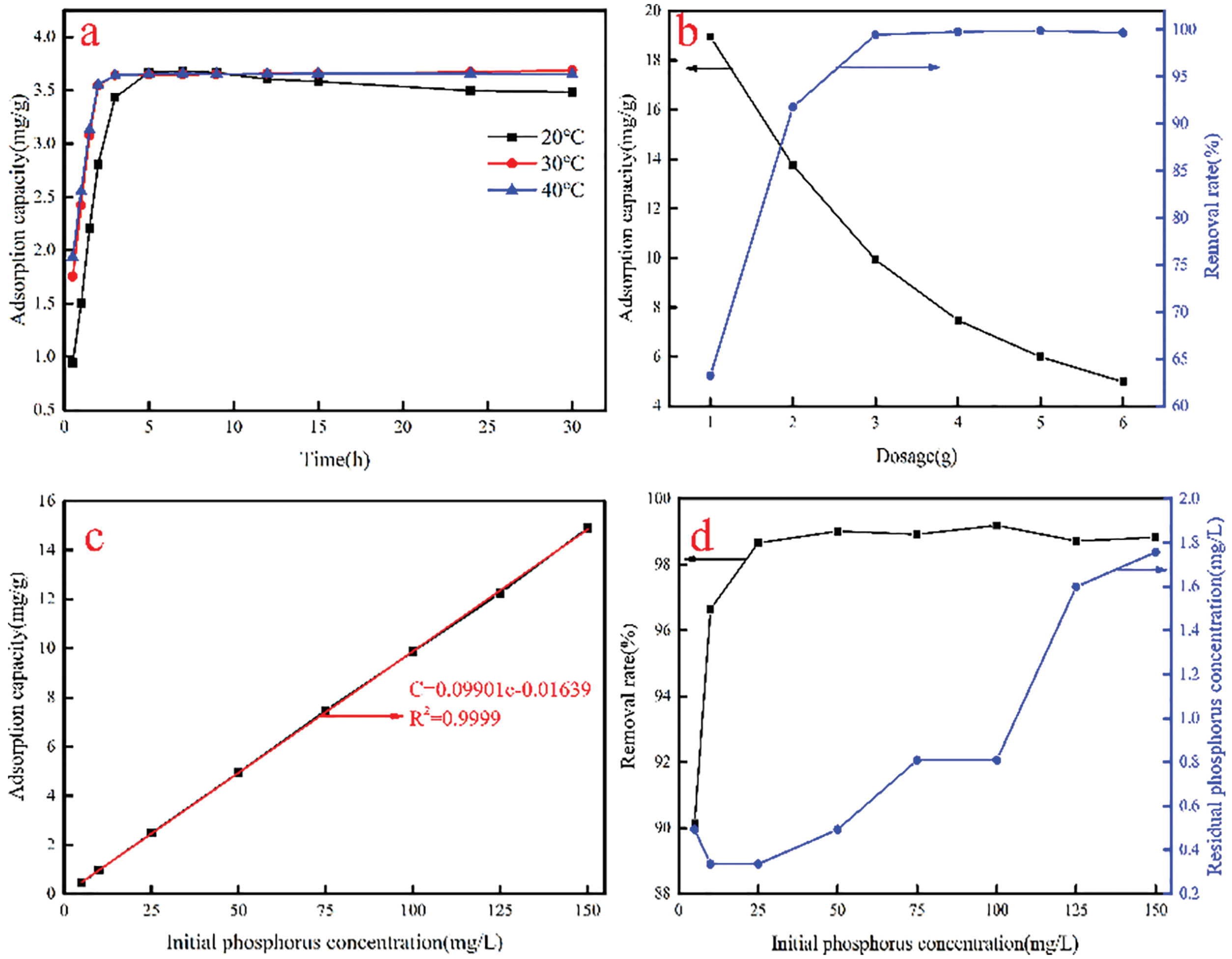

Figure 5: Adsorption curves of FB-OS under different conditions (a is the adsorption curves of FB-OS under different temperatures, b is the adsorption curves of FB-OS under different dosages, c is the absorption curves of FB-OS under different phosphorus concentration, d is the removal rate and residual phosphorus concentration curves of FB-OS under different phosphorus concentration)

3.2.3 Effect of Different Phosphorus Concentrations on Adsorption Properties of FB-OS

Phosphorus solution (250 mL 300 mg/L) was prepared, and 1.0 g FB-OS was added into above solution. At room temperature, FB-OS statically adsorbed phosphorus from solution. After 14th, 15th, and 16th days, phosphorus concentration in the solution was almost the same. The maximum adsorption capacity of the sample was calculated to be 48.31 mg/g.

In order to study the effect of different initial phosphorus concentrations on the phosphorus removal effect of FB-OS, 100 mL of aqueous solution with different phosphorus concentrations was prepared, 1.0 g FB-OS was added into above phosphorus solution, at room temperature FB-OS statically adsorbed, test water samples were taken after 2 d, and phosphorus concentration was measured, the results were shown in Fig. 5c. The figure showed that under the experimental conditions, the adsorption capacity increased linearly with the phosphorus concentration increasing. This was due to FB-OS having sufficient active sites, PO_4^{3-} was more, the probability of contact with the active site was greater, and the adsorption capacity of FB-OS was greater [50]. Fig. 5d also showed that the removal rate increased first and then remained unchanged with the increase of initial phosphorus concentration. The removal rates of all experiments were in the range of 90.14%~99.19%. When the phosphorus concentration was 5~100 mg/L, the phosphorus concentration was less than 1 mg/L after phosphorus removal. And 100~150 mg/L, residual phosphorus was 1.60~1.76 mg/L. Increase in the adsorbent, the residual phosphorus concentration was expected to be reduced to 1 mg/L. In conclusion, FB-OS could reduce phosphorus concentration to less than 1 mg/L.

3.2.4 Adsorption Dynamics Fitting Results and Analysis

In order to further explore the adsorption behavior of FB-OS, the adsorption curve of FB-OS at 30°C (Fig. 5a) was fitted by pseudo-first-order (PFO) and pseudo-second-order kinetic equations (PSO), the results were shown in Table 1 and Fig. 6. It can be seen from Table 1 that PSO had the best fitting result ($R^2 = 0.995$), and its predicted saturated adsorption capacity (q_e) was 3.96 mg/g, which was close to the experimental adsorption capacity (q_{ec}) of 3.66 mg/g. In addition, PSO theory is based on divalent metal ions adsorbing polar groups (aldehydes, ketones and phenols), this is similar to Ca^{2+} adsorbing PO_4^{3-} (HPO_4^{2-} and $H_2PO_4^-$) in the paper [51]. Meanwhile, according to "3.1.3" it could be seen that there were chemical reactions in the process of phosphorus removal. In summary, it was reasonable to use PSO to explain the adsorption behavior of FB-OS to phosphorus. PSO generally contains surface adsorption, outer film diffusion and intraparticle diffusion process. The surface adsorption (i.e., surface chemical reaction) rate is fast, while the outer film diffusion and intraparticle diffusion rate are slow [52]. Therefore, the adsorption rate is controlled by the outer film diffusion and intraparticle diffusion.

Table 1: Different kinetic equations fitting effects of FB-OS adsorption curve at 30°C

Kinetic equations	q_{ec} (mg/g)	q_e (mg/g)	k_1 (h^{-1})	k_2 (g/(mg·h))	R^2
Pseudo-first-order rate equation	3.66	1.316	0.840	–	0.772
Pseudo-second-order rate equation	3.66	3.96	–	0.65	0.995

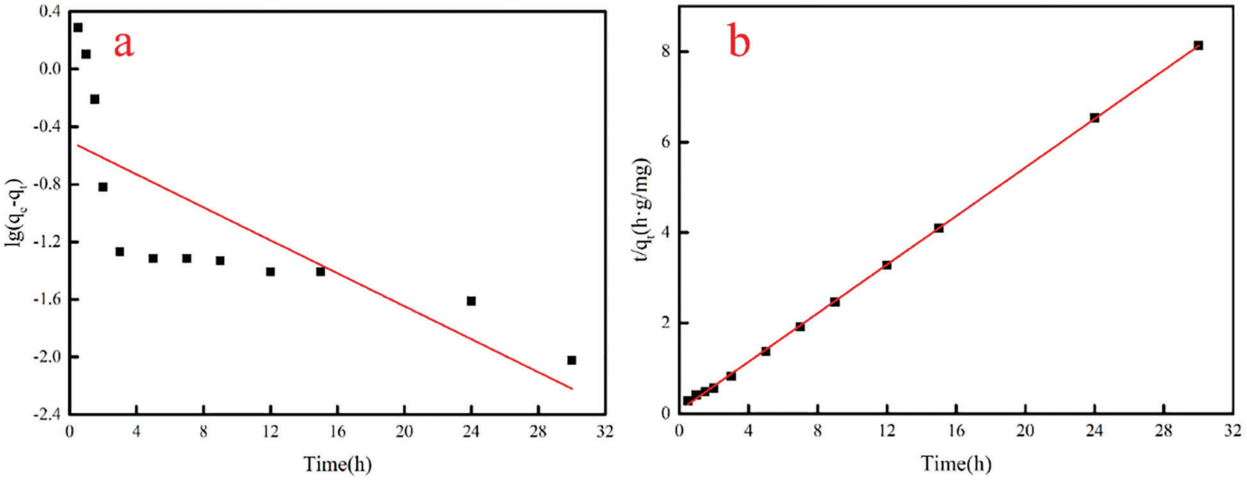

Figure 6: PFO and PSO fitting results of FB-OS at 30°C (a is the PFO fitting result, b is the PSO fitting result)

Based on the literature [50,52] and PSO model, the adsorption process can commonly be divided into three stages: rapid adsorption, slow adsorption, and equilibrium. In Fig. 5a, at 30°C, it can be seen that 0~4 h was the rapid adsorption stage. In this process, there were a large number of PO_4^{3-} in the aqueous solution, and FB-OS had a large number of unreacted active sites. The FB-OS was added to the phosphorus solution, and the phosphorus solution wetted the composite material and entered the interior of the composite material along the gap. And then, the rich Ca^{2+} in the FB-OS could react rapidly with PO_4^{3-} to form $Ca_3(PO_4)_2$, etc. PO_4^{3-} in phosphorus solution was quickly fixed. From 4 to 5 h, it was the slow adsorption stage. Relative to the rapid adsorption stage, during this process, phosphorus concentration in water was significantly reduced, and the concentration difference between internal and external phosphorus of FB-OS also was significantly reduced. Meanwhile, a large amount of amorphous calcium phosphate was generated on the surface and inside of FB-OS (Figs. 3d, 3e), which may be hindering the diffusion of phosphorus solution in the material. These led to a slowing down of the phosphate transfer rate inside and outside the particle. At the same time, part of active sites of FB-OS were inactivated after binding to PO_4^{3-}. Under the combined action of various factors, the adsorption rate of FB-OS decreased. In addition, a large amount of $Ca_3(PO_4)_2$ was generated at this stage, which led to the desorption rate increased. However, the adsorption rate at this stage was still greater than the desorption rate. As the adsorption proceeds, the adsorption rate gradually slowed, and the desorption rate gradually increased. When the adsorption and desorption rates were the same, FB-OS reached the adsorption equilibrium, and phosphorus was no longer adsorbed in water. This was the equilibrium stage.

4 Conclusion

Iron-pillared bentonite was prepared by modifying calcium bentonite with iron-pillared liquid, and then the composite material was prepared by mixing, granulating and calcining the iron-pillared bentonite and oyster shell powder. The characterization results showed that FB-OS generated CaO under high-temperature calcination. The maximum bending stress of FB-OS was 43.7 N, and the compressive strength was 0.927 MPa. SEM analysis showed that the structure of FB-OS was compact, but there were gaps in it. The phosphorus removal test showed that the maximum adsorption capacity of FB-OS was 48.31 mg/g, and the phosphorus removal rate was more than 90%. After phosphorus removal, SEM observed that spherical products were produced on the surface and inside FB-OS, it was speculated that they were amorphous calcium phosphate. Analysis indicated that chemical adsorption existed in the process of phosphorus removal, and the process could be expressed by PSO model: $q_t = \frac{10.193t}{1 + 2.574t}$ (R^2 = 0.995). The adsorption rate was mainly controlled by outer film diffusion and intraparticle diffusion.

Funding Statement: This work was supported by the Project of Guangdong Academy of Building Research Group Co., Ltd., China (No. 0100RDY2022D0000036).

Conflicts of Interest: We declare that we do not have any commercial or associative interest that represents a conflict of interest in connection with the work submitted.

References

1. Botta, R., Asche, F., Borsum, J. S., Camp, E. V. (2020). A review of global oyster aquaculture production and consumption. *Marine Policy, 117,* 103952. https://doi.org/10.1016/j.marpol.2020.103952
2. Çatlı, A., Bozkurt, M., Küçükyılmaz, K., Çınar, M., Bintas, E. et al. (2012). Performance and egg quality of aged laying hens fed diets supplemented with meat and bone meal or oyster shell meal. *South African Journal of Animal Science, 42(1)*. https://doi.org/10.4314/sajas.v42i1.9
3. Chilakala, R., Thannaree, C., Shin, E. J., Thenepalli, T., Ahn, J. W. (2019). Sustainable solutions for oyster shell waste recycling in Thailand and the Philippines. *Recycling, 4(3),* 35. https://doi.org/10.3390/recycling4030035
4. Ruslan, H. N., Muthusamy, K., Mohsin, S. M. S., Jose, R., Omar, R. (2021). Oyster shell waste as a concrete ingredient: A review. *Materials Today: Proceedings, 48,* 713–719. https://doi.org/10.1016/j.matpr.2021.02.208

5. Bassi, L. S., Durau, J. F., Zavelinski, V. A. B., Krabbe, E. L., Surek, D. et al. (2022). Particle size of oyster shell meal and calcium: Phosphorus ratios in broiler diets. *Ciência Rural, 52*. https://doi.org/10.1590/0103-8478cr20210524
6. Xu, Z., Valeo, C., Chu, A., Zhao, Y. (2021). The efficacy of whole oyster shells for removing copper, zinc, chromium, and cadmium heavy metal ions from stormwater. *Sustainability, 13(8),* 4184. https://doi.org/10.3390/su13084184
7. Lee, J. I., Kang, J. K., Oh, J. S., Yoo, S. C., Lee, C. G. et al. (2021). New insight to the use of oyster shell for removing phosphorus from aqueous solutions and fertilizing rice growth. *Journal of Cleaner Production, 328,* 129536. https://doi.org/10.1016/j.jclepro.2021.129536
8. Park, W. H., Polprasert, C. (2008). Roles of oyster shells in an integrated constructed wetland system designed for P removal. *Ecological Engineering, 34(1),* 50–56. https://doi.org/10.1016/j.ecoleng.2008.05.014
9. Martins, M. C., Santos, E. B., Marques, C. R. (2017). First study on oyster-shell-based phosphorous removal in saltwater—A proxy to effluent bioremediation of marine aquaculture. *Science of the Total Environment, 574,* 605–615. https://doi.org/10.1016/j.scitotenv.2016.09.103
10. Huh, J. H., Choi, Y. H., Lee, H. J., Choi, W. J., Ramakrishna, C. et al. (2016). The use of oyster shell powders for water quality improvement of lakes by algal blooms removal. *Journal of the Korean Ceramic Society, 53(1),* 1–6. https://doi.org/10.4191/kcers.2016.53.1.1
11. Qiu, L., Zheng, P., Zhang, M., Yu, X., Abbas, G. (2015). Phosphorus removal using ferric–calcium complex as precipitant: Parameters optimization and phosphorus-recycling potential. *Chemical Engineering Journal, 268,* 230–235. https://doi.org/10.1016/j.cej.2014.12.107
12. Toor, U. A., Kim, D. J. (2019). Effect of pH on phosphorus (P) dissolution and recovery from polyaluminum chlorides (PAC) sludge. *Journal of Environmental Management, 239,* 142–149. https://doi.org/10.1016/j.jenvman.2019.03.049
13. Feng, Y., Luo, Y., He, Q., Zhao, D., Zhang, K. et al. (2021). Performance and mechanism of a biochar-based Ca-la composite for the adsorption of phosphate from water. *Journal of Environmental Chemical Engineering, 9(3),* 105267. https://doi.org/10.1016/j.jece.2021.105267
14. Alexander, J. A., Ahmad Zaini, M. A., Surajudeen, A., Aliyu, E. N. U., Omeiza, A. U. (2019). Surface modification of low-cost bentonite adsorbents—A review. *Particulate Science and Technology, 37(5),* 538–549. https://doi.org/10.1080/02726351.2018.1438548
15. Cheng, H., Zhu, Q., Xing, Z. (2019). Adsorption of ammonia nitrogen in low temperature domestic wastewater by modification bentonite. *Journal of Cleaner Production, 233,* 720–730. https://doi.org/10.1016/j.jclepro.2019.06.079
16. Mi, H., Yi, L., Wu, Q., Xia, J., Zhang, B. (2021). Preparation of high-strength ceramsite from red mud, fly ash, and bentonite. *Ceramics International, 47(13),* 18218–18229. https://doi.org/10.1016/j.ceramint.2021.03.141
17. Ma, G., Zhang, H., Ji, Z., Tan, Y. (2021). Comparison of the swelling pressure of bentonite pellet-contained materials and powder. *Construction and Building Materials, 281,* 122531. https://doi.org/10.1016/j.conbuildmat.2021.122531
18. Bertella, F., Pergher, S. B. C. (2015). Pillaring of bentonite clay with Al and Co. *Microporous and Mesoporous Materials, 201,* 116–123. https://doi.org/10.1016/j.micromeso.2014.09.013
19. Xu, H., Hu, X., Chen, Y., Li, Y., Zhang, R. et al. (2021). Cd(II) and Pb(II) absorbed on humic acid-iron-pillared bentonite: Kinetics, thermodynamics and mechanism of adsorption. *Colloids and Surfaces A: Physicochemical and Engineering Aspects, 612,* 126005. https://doi.org/10.1016/j.colsurfa.2020.126005
20. Yang, W., Lin, S., Fang, R., Feng, J. L. (2009). Research on manufacture of the Fe-pillaring bentonite and its absorption properties of Cr(VI). *Journal of Shenyang Jianzhu University (Natural Science), 25(5),* 968–973.
21. Liu, X., Shen, F., Smith, R. L., Qi, X. (2019). Black liquor-derived calcium-activated biochar for recovery of phosphate from aqueous solutions. *Bioresource Technology, 294,* 122198. https://doi.org/10.1016/j.biortech.2019.122198
22. Cheng, G., Li, Q. H., Su, Z., Sheng, S., Fu, J. (2018). Preparation, optimization, and application of sustainable ceramsite substrate from coal fly ash/waterworks sludge/oyster shell for phosphorus immobilization in

constructed wetlands. *Journal of Cleaner Production, 175,* 572–581. https://doi.org/10.1016/j.jclepro.2017.12.102

23. Ho, Y. S., Mckay, G. (1998). A comparison of chemisorption kinetic models applied to pollutant removal on various sorbents. *Process Safety and Environmental Protection, 76(4),* 332–340. https://doi.org/10.1205/095758298529696
24. Revellame, E. D., Fortela, D. L., Sharp, W., Hernandez, R., Zappi, M. E. (2020). Adsorption kinetic modeling using pseudo-first order and pseudo-second order rate laws: A review. *Cleaner Engineering and Technology, 1,* 100032. https://doi.org/10.1016/j.clet.2020.100032
25. Tran, H. N., You, S. J., Hosseini-Bandegharaei, A., Chao, H. P. (2017). Mistakes and inconsistencies regarding adsorption of contaminants from aqueous solutions: A critical review. *Water Research, 120,* 88–116. https://doi.org/10.1016/j.watres.2017.04.014
26. Patle, T. K., Shrivas, K., Kurrey, R., Upadhyay, S., Jangde, R. et al. (2020). Phytochemical screening and determination of phenolics and flavonoids in *Dillenia pentagyna* using UV–vis and FTIR spectroscopy. *Spectrochimica Acta Part A: Molecular and Biomolecular Spectroscopy, 242,* 118717. https://doi.org/10.1016/j.saa.2020.118717
27. Yuan, P., Annabi, B., Qi, T. A., Mingde, F. A., Liu, Z. et al. (2008). A combined study by XRD, FTIR, TG and HRTEM on the structure of delaminated Fe-intercalated/pillared clay. *Journal of Colloid and Interface Science, 324(1–2),* 142–149. https://doi.org/10.1016/j.jcis.2008.04.076
28. Banu, H. A. T., Karthikeyan, P., Vigneshwaran, S., Meenakshi, S. (2020). Adsorptive performance of lanthanum encapsulated biopolymer chitosan-kaolin clay hybrid composite for the recovery of nitrate and phosphate from water. *International Journal of Biological Macromolecules, 154,* 188–197. https://doi.org/10.1016/j.ijbiomac.2020.03.074
29. Pentrák, M., Hronský, V., Pálková, H., Uhlík, P., Komadel, P. et al. (2018). Alteration of fine fraction of bentonite from kopernica (Slovakia) under acid treatment: A combined XRD, FTIR, MAS NMR and AES study. *Applied Clay Science, 163,* 204–213. https://doi.org/10.1016/j.clay.2018.07.028
30. Awwad, A., Shammout, M., Amer, M. (2021). $Fe(OH)_3$/kaolinite nanoplatelets: Equilibrium and thermodynamic studies for the adsorption of Pb(II) ions from aqueous solution. *Social Science Electronic Publishing, 3,* 90–102.
31. You, K., Feng, L., Fan, L., Song, P., Han, X. et al. (2020). The controlled release of phosphorus in water by magnet zirconium modified oyster shell. *Acta Scientiae Circumstantiae, 40,* 2486–2495. https://doi.org/10.13671/j.hjkxxb.2020.0036
32. Balmain, J., Hannoyer, B., Lopez, E. (2015). Fourier transform infrared spectroscopy (FTIR) and X-ray diffraction analyses of mineral and organic matrix during heating of mother of pearl (nacre) from the shell of the mollusc pinctada maxima. *Journal of Biomedical Materials Research, 48(5),* 749–754. https://doi.org/10.1002/(ISSN)1097-4636
33. Huang, Y. (2010). *Phosphours removal by Pulverized Oyster shell (Master Thesis)*. Fuzhou University, Fuzhou, China.
34. Bandipally, S., Cherian, C., Arnepalli, D. N. (2018). Characterization of lime-treated bentonite using thermogravimetric analysis for assessing its short-term strength behaviour. *Indian Geotechnical Journal, 48(3),* 393–404. https://doi.org/10.1007/s40098-018-0305-7
35. Pereira da Costa, F., Rodrigues da Silva Morais, C., Rodrigues, A. M. (2020). Sustainable glass-ceramic foams manufactured from waste glass bottles and bentonite. *Ceramics International, 46,* 17957–17961. https://doi.org/10.1016/j.ceramint.2020.04.107
36. Yang, X. X., Li, Y. M., Gao, H. M., Wang, C. Y., Zhang, X. H. et al. (2018). One-step fabrication of chitosan-$Fe(OH)_3$ beads for efficient adsorption of anionic dyes. *International Journal of Biological Macromolecules, 117,* 30–41. https://doi.org/10.1016/j.ijbiomac.2018.05.137
37. Garcia-Mora, A. M., Torres-Palma, R. A., García, H., Hidalgo-Troya, A., Galeano, L. A. (2021). Removal of dissolved natural organic matter by the Al/Fe pillared clay-activated-catalytic wet peroxide oxidation: Statistical multi-response optimization. *Journal of Water Process Engineering, 39,* 101755. https://doi.org/10.1016/j.jwpe.2020.101755

38. Souza, A. D. V., Arruda, C. C., Fernandes, L., Antunes, M. L. P., Kiyohara, P. K. et al. (2015). Characterization of aluminum hydroxide ($Al(OH)_3$) for use as a porogenic agent in castable ceramics. *Journal of the European Ceramic Society, 35(2),* 803–812. https://doi.org/10.1016/j.jeurceramsoc.2014.09.010
39. Mercury, J. M. R., Pena, P., de Aza, A. H., Sheptyakov, D., Turrillas, X. (2006). On the decomposition of synthetic gibbsite studied by Neutron Thermodiffractometry. *Journal of the American Ceramic Society, 89(12),* 3728–3733. https://doi.org/10.1111/j.1551-2916.2006.01191.x
40. Beruto, D. T., Botter, R., Lagazzo, A., Finocchio, E. (2012). Calcium oxides for CO_2 capture obtained from the thermal decomposition of $CaCO_3$ particles coprecipitated with Al^{3+} ions. *Journal of the European Ceramic Society, 32(2),* 307–315. https://doi.org/10.1016/j.jeurceramsoc.2011.08.022
41. Patel, S., Kundu, S., Halder, P., Rickards, L., Paz-Ferreiro, J. et al. (2019). Thermogravimetric analysis of biosolids pyrolysis in the presence of mineral oxides. *Renewable Energy, 141,* 707–716. https://doi.org/10.1016/j.renene.2019.04.047
42. Zhou, Z., Xu, Q., Wu, Z., Fang, X., Zhong, Q. et al. (2023). Preparation and characterization of clay-oyster shell composite adsorption material and its application in phosphorus removal from wastewater. *Sustainable Chemistry and Pharmacy, 32,* 101023. https://doi.org/10.1016/j.scp.2023.101023
43. Zhang, H., Tong, Z., Wei, T., Tang, Y. (2012). Sorption characteristics of Pb(II) on alkaline Ca-bentonite. *Applied Clay Science, 65–66,* 21–23. https://doi.org/10.1016/j.clay.2012.06.010
44. Masood, B., Elahi, A., Barbhuiya, S., Ali, B. (2020). Mechanical and durability performance of recycled aggregate concrete incorporating low calcium bentonite. *Construction and Building Materials, 237,* 117760. https://doi.org/10.1016/j.conbuildmat.2019.117760
45. Ding, Y., Tang, S., Han, R., Zhang, S., Pan, G. et al. (2020). Iron oxides nanobelt arrays rooted in nanoporous surface of carbon tube textile as stretchable and robust electrodes for flexible supercapacitors with ultrahigh areal energy density and remarkable cycling-stability. *Scientific Reports, 10(1),* 11023. https://doi.org/10.1038/s41598-020-68032-z
46. Zhou, J., Li, D., Zhao, Z., Song, X., Huang, Y. et al. (2020). Phosphorus immobilization by the surface sediments under the capping with new calcium peroxide material. *Journal of Cleaner Production, 247,* 119135. https://doi.org/10.1016/j.jclepro.2019.119135
47. Lei, Y., Saakes, M., van der Weijden, R. D., Buisman, C. J. N. (2020). Electrochemically mediated calcium phosphate precipitation from phosphonates: Implications on phosphorus recovery from non-orthophosphate. *Water Research, 169,* 115206. https://doi.org/10.1016/j.watres.2019.115206
48. Chen, W. T., Lin, C. W., Shih, P. K., Chang, W. L. (2012). Adsorption of phosphate into waste oyster shell: Thermodynamic parameters and reaction kinetics. *Desalination and Water Treatment, 47(1–3),* 86–95. https://doi.org/10.1080/19443994.2012.696800
49. Tran, T. T., Tran, N., Sugiyama, S., Liu, J. C. (2020). Enhanced phosphate removal by thermally pretreated waste oyster shells. *Journal of Material Cycles and Waste Management, 23(4),* 1–9.
50. Chen, J., Cai, Y., Clark, M., Yu, Y. (2013). Equilibrium and kinetic studies of phosphate removal from solution onto a hydrothermally modified oyster shell material. *PLoS One, 8(4),* e60243. https://doi.org/10.1371/journal.pone.0060243
51. Qiu, H., Lv, L., Pan, B. C., Zhang, Q. J., Zhang, W. M. et al. (2009). Critical review in adsorption kinetic models. *Journal of Zhejiang University, 10(5),* 716–724. https://doi.org/10.1631/jzus.A0820524
52. Lima, É. C., Adebayo, M. A., Machado, F. M. (2015). Kinetic and equilibrium models of adsorption. In: Bergmann, C., Machado, F. (Eds.), *Carbon nanomaterials as adsorbents for environmental and biological applications. Carbon nanostructures*, pp. 33–69. Cham: Springer. https://doi.org/10.1007/978-3-319-18875-1_3